Received: 1 June 2021 | Revised: 31 August 2021 | Accepted: 18 October 2021

DOI: 10.1002/suco.202100350

ARTICLE

fib CEB-FIP WILEY

Rotation and moment redistribution capacity of fiber-reinforced concrete beams: Parametric analysis and code compliance

Alejandro Nogales[1] | **Nikola Tošić**[2] | **Albert de la Fuente**[2]

[1]Smart Engineering Ltd., UPC Spin-Off. Civil and Environmental Engineering Department, Universitat Politècnica de Catalunya (UPC), Barcelona, Spain

[2]Civil and Environmental Engineering Department, Universitat Politècnica de Catalunya (UPC), Barcelona, Spain

Correspondence
Alejandro Nogales, Smart Engineering Ltd., UPC Spin-Off. Civil and Environmental Engineering Department, Universitat Politècnica de Catalunya (UPC), Barcelona, Spain.
Email: alejandro.nogales@upc.edu

Funding information
Ministerio de Ciencia e Innovación, Grant/Award Number: DI-17-09390; Ministerio de Economía, Industria y Competitividad, Gobierno de España, Grant/Award Number: PID2019-108978RB-C32

Abstract

Fiber-reinforced concrete (FRC) has been proved to be a competitive solution for structural purposes. Extensive research has highlighted the benefits of adding fibers on the post-cracking strength, reduced crack spacing and crack width, and improved durability, among others. However, these aspects are related to serviceability limit states, and significant work remains to be done in terms of ultimate limit state behavior of FRC members. As recent publications have emphasized, reinforced concrete beams with low reinforcement ratios may result in a reduction of deformation capacity and, hence, to a loss of ductility. To further investigate this topic, this paper presents the results of a numerical parametric study of simply and continuous supported hybrid-reinforced concrete (HRC) beams made with different amounts of fibers and reinforcement ratios. The deformation, rotational, and moment redistribution capacity of those were assessed by means of a finite-element model previously calibrated using experimental results available in the literature. The results showed that there is a significant reduction of rotation capacity and moment redistribution for lightly reinforced (hybrid) members. Finally, the paper contains practical recommendations in terms of minimum reinforcement ratios that guarantee adequate rotation and redistribution capacity of HRC members. As such, the results of this study can provide a contribution toward more reliable structural designs of HRC members.

KEYWORDS

deformation capacity, ductility, fiber-reinforced concrete, ultimate limit state

1 | INTRODUCTION

The increasing use of fiber-reinforced concrete (FRC) in those structural members for which flexure is the governing design condition has given rise to questions

Discussion on this paper must be submitted within two months of the print publication. The discussion will then be published in print, along with the authors' closure, if any, approximately nine months after the print publication.

regarding the deformation capacity of such elements. As it has been previously shown, the addition of structural fibers tends to reduce crack spacing, crack widths, and deflections, while, at the same time, it increases stiffness and the load-bearing capacity of flexural members.[1–4] Therefore, the improvements are mostly related to serviceability limit state (SLS) performance. These aspects allow engineers to use optimal combinations of fibers and longitudinal reinforcement that can maintain the same load-bearing capacity as reinforced concrete (RC), but with lower reinforcement ratios (ρ_s) minimizing cracks and deflections while reducing building time and costs. Nevertheless, as it has been outlined in References 5–8 that the combination of fibers and conventional reinforcement (known as hybrid-reinforced concrete [HRC]) may lead to failure at lower deformations compared with those corresponding to elements without fibers, hence compromising both the bearing capacity and degree of ductility at the ultimate limit state (ULS).

Experimental research carried out on simply supported beams combining different values of ρ_s, and fiber volume fraction (V_f)[8–12] provided results that confirm this loss of deformation capacity, relating it directly to rotational capacity. The reported loss of rotation capacity was caused by crack localization, resulting in failure of the conventional steel rebars at lower deformations, particularly for low values of ρ_s (i.e., <0.5%) that are close to the minimum reinforcement ratio necessary for avoiding brittle failure. Other tests conducted on simply supported beams with $\rho_s \geq 0.5\%$ showed that the beam deformation capacity was unaltered, without any crack localization.[13,14] These outcomes are of paramount importance, as the combination of structural fibers with low amounts of conventional reinforcement is frequently used in several structural typologies (i.e., industrial flooring,[15,16] precast concrete segments for tunnel linings,[17] and sewerage pipes[18,19]), and this embrittlement effect could jeopardize the ductile response expected in case of failure. In this regard, the previous experimental research has been focused on specific magnitudes of ρ_s and FRC strength classes, and consequently, the conclusions and recommendations derived from the results should be limited accordingly.

Of particular importance, in this regard, is the ability of statically indeterminate structures to redistribute moments. It allows the structure to transfer forces away from critical sections, allowing to reach higher loads and eventually leading to more ductile failure; a feature of special importance in seismically active regions.[20] Comprehensive research has been carried out regarding this topic, since the capacity of the non-critical sections can be used, allowing the designer to optimize reinforcement requirements and, therefore, costs.[21] Moment redistribution occurs at all limit states due to the longitudinal variation in stiffness, and the most rigid sections tend to absorb more forces than less rigid.[22] When a section cracks, its stiffness is affected, and it takes smaller moments under increasing loads than it would have if it had not cracked; the moment redistribution results in a change in the distribution of bending moments obtained from a theoretical linear elastic analysis.[23–27] At ULS, moment redistribution occurs due to the formation and gradual rotation of plastic hinge regions and has also been shown to be highly dependent on the stiffness or flexural rigidity of the non-hinge regions.[24,28,29]

The large number of experimental results regarding this topic has allowed the incorporation of moment redistribution in design guidelines and codes. The margin of moment redistribution allowed in national and international codes[30–34] depends primarily, apart from the structure typology, on the rotation capacity of plastic hinge regions. For continuous beams, the maximum moment redistribution allowed is 30% for Eurocode 2 (EC2),[33] the *fib* Model Code 2010 (MC2010),[34] and the Australian code,[31] whereas it is limited to 15% for the Spanish code EHE-08[32] and 20% for American Concrete Institute's Building Code ACI 318-14.[30]

Regarding moment redistribution in HRC members, experimental tests conducted on statically indeterminate HRC/FRC two-span continuous beams are gathered in Table 1. Küsel and Kearsley[37] found that the addition of fibers led to crack localization, reducing the deformation capacity and leading to less moment redistribution; this being more evident in FRC element with strain-softening response at the post-cracking regime. Contrarily, Mahmood et al.[36] observed no signs of crack localization when comparing RC and HRC beams with ρ_s of 0.69% and 1.38%. Finally, Visintin et al.[35] tested ultrahigh performance fiber-reinforced concrete (UHPFRC) with large fiber contents. The results showed that fibers provided enough ductility to the concrete compressive behavior that shifted the failure mode from concrete crushing to reinforcement rupture, allowing the beam to reach larger deformation, and thus, no significant change in moment redistribution was reported.

In view of the results of the studies presented in this section, further study is required for HRC flexural members at ULS, since there is uncertainty of its dependence on different values of ρ_s and FRC residual strength.[38] Hence, there is a pressing need to evaluate the influence of the use of fibers in the deformation capacity (plastic rotation) that could compromise the moment redistribution phenomenon in HRC elements. Particularly, it is of paramount importance to investigate members with $\rho_s < 0.5\%$, since the addition of fibers to RC members is typically viewed as a way of optimizing (eventually reducing) longitudinal reinforcement.

TABLE 1 Previous research focused on HRC and FRC two-span continuous beams

Material	f_{cm} [MPa]	Cross-section [mm^2]	Span length [mm]	V_f [%]	ρ_s [%]	Tests	Distance of load from central support	Ref.
UHPFRC	156	200 × 220	2 × 2500	2.08	1.28–1.94	4	0.5·L	35
HRC	40	250 × 400	2 × 4000	0.38 0.76	0.69 1.38	6	0.5·L	36
HRC RC[a] FRC	80	200 × 100	2 × 2250	0.00 0.76 1.51 2.20	0.7 1.4 2.2	15	0.44·L	37

[a]RC—reinforced concrete.

In order to achieve this goal, a parametric analysis on simply supported beams and on statically indeterminate continuous beams with varying FRC residual strength classes, according to MC2010,[34] and varying longitudinal reinforcement ratios were performed in this study. The specific objectives of this study are twofold: (1) to evaluate the deformation and rotational capacity of simply supported HRC beams and (2) to quantify the moment redistribution for two-span continuous HRC beams. To this end, a finite-element model (FEM) was calibrated and validated using results from experimental programs reported in the literature and then applied to two comprehensive parametric studies. The obtained results were analyzed, and design-oriented recommendations are provided to be potentially taken into consideration for future revisions of the MC2010[34] and other national/international guidelines.

2 | CALIBRATION AND VALIDATION OF THE NUMERICAL MODEL FOR HRC BEAMS

The FEM was first calibrated on real-scale continuous beams reported in Reference 36. To verify the adequacy of the model to measure the moment redistribution phenomenon, two additional experimental programs were simulated.[35,37] Finally, the FEM was applied to simply supported beams tested by Bosco and Debernardi[39] to compare the results in terms of deformation capacity and plastic rotation.

2.1 | Selection of constitutive models

The compressive stress–strain (σ–ε) and tensile stress–crack opening (σ–w) relationships were established according to *fib* MC2010[34] that are used (see Figure 1). Flexural residual strengths (f_R) can be obtained from the three point bending test on notched beams according to EN 14651,[40] where f_{R1} and f_{R3} stand for the residual strengths for a crack mouth opening displacement (CMOD) of 0.5 and 2.5 mm, respectively. Mean values of each of the involved mechanical variables are considered for the numerical simulations.

The concrete damage plasticity (CDP) model available in ABAQUS[41] is used. This software presents a versatile tool to successfully model a wide range phenomenon of concrete structure behavior, as evidenced by numerous published studies.[42–45] The CDP model is a continuum, smeared crack, plasticity-based, damage model for concrete. In smeared crack models, the damage zone is assumed to coincide with the FE dimensions. The model assumes that the main two failure mechanisms for concrete are tensile cracking and compressive crushing. To model the concrete behavior, the input data required are uniaxial σ–ε curves for compression and tension, see Figure 1. However, to overcome mesh dependence, the σ–w tensile curve was used instead. In this regard, the characteristic length (L_{ch}) was assumed to be the size of the FE. The CDP magnitude of the parameters adopted for all the simulations was those proposed in ABAQUS User's Manual[41] for plain concrete, except those for the dilation angle, which was determined by means of a sensitivity analysis.

2.2 | HRC model calibration

The experimental study carried out by Mahmood et al.[36] on flexural performance of steel fiber-reinforced (SFRC) concrete beams was used for the model calibration. Full-scale two-span continuous reinforced concrete beams were tested using steel reinforcement ratios (ρ_s) of 0.69% and 1.38%, and 0, 30, and 60 kg/m^3 of steel fibers (corresponding to V_f of 0.38% and 0.76%), the combination of the parameters leading to a total of six beams. The steel fibers had a length and diameter of 60 and 0.9 mm,

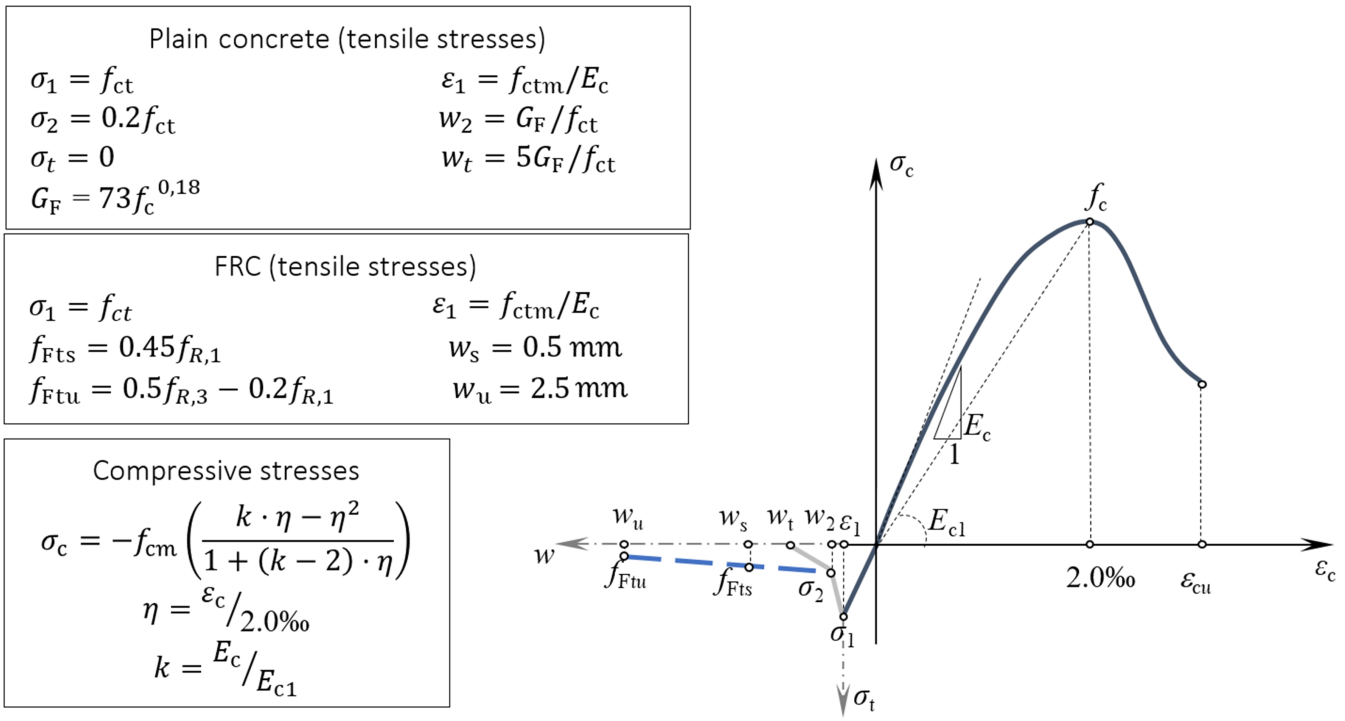

FIGURE 1 Constitutive equations for concrete; σ–ε for compression and σ–w for tension

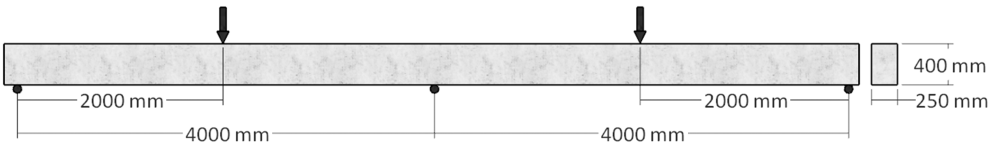

FIGURE 2 Mahmood et al.[36] continuous beam experimental test setup

respectively. The tested beams had a clear span of 4000 mm, with a cross-sectional height and width of 400 and 250, respectively, as shown in Figure 2, with load evenly applied to both midspans.

The mean compressive concrete strength (f_{cm}) was 60 MPa. Furthermore, three point bending tests according to EN 14651[40] were conducted to measure the tensile post-cracking behavior of SFRC; for the purposes of this study, the flexural strength test results were used to derive the stress–crack width (σ–w) tensile constitutive curves according to MC2010.[34] The uniaxial stress–strain (σ–ε) curves of the steel bars were also provided in Reference 36 with a yield strength (f_y) equal to 540, an ultimate strength (f_u), and an ultimate strain (ε_{su}) equal to 400 MPa and 0.18, respectively, and a maximum strength (f_{max}) of 613 MPa (at a strain of 0.11).

Two beams were used for the model calibration: B00 (−30) and B30(−30) at Reference 36, hereafter referred to as B0 and B30. Beam B0 is an RC, and beam B30 is an HRC beam with V_f equal to 0.38% (30 kg/m^3 of steel fibers). For both beams, the reinforcement arrangement consisted of two 20-mm diameter bars at the top and bottom layers (with a concrete cover of 30 mm) along the beam length and an additional bar at the midspans (1250 mm at either side of the midspan), which corresponded to $\rho_s = 1.05\%$, as shown in Figure 3. The reinforcement configuration was adopted by the authors, so a 30% moment redistribution was produced from the hogging to the sagging region (from the support to the midspan region). In addition, 10-mm diameter stirrups placed every 200 mm as transversal reinforcement. The FE mesh considered for the numerical analysis and the boundary conditions can be seen in Figure 3a. The mesh is comprised by 7800 elements: 6500 50-mm size eight-node solid linear hexahedral solid elements (C3D8R) were used for modeling concrete, whereas the steel bars were modeled with 1300 linear T3D2 elements assuming a perfect bond between steel and concrete, using an embedded condition. The middle support was fixed in both x and y directions ($u_x = u_y = 0$), and the external supports were fixed only in the vertical direction ($u_y = 0$), both constraints applied along a line. The analysis was performed by first applying self-weight and then an increasing load applied by deflection control, which was

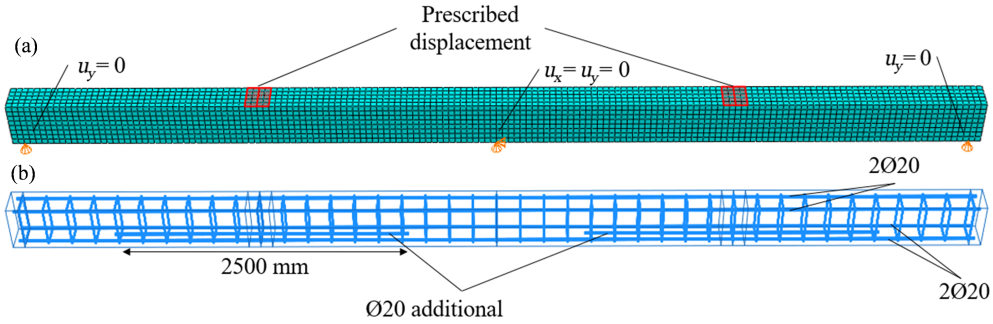

FIGURE 3 FEM for B0 and B30 (a) mesh and boundary conditions and (b) reinforcement arrangement

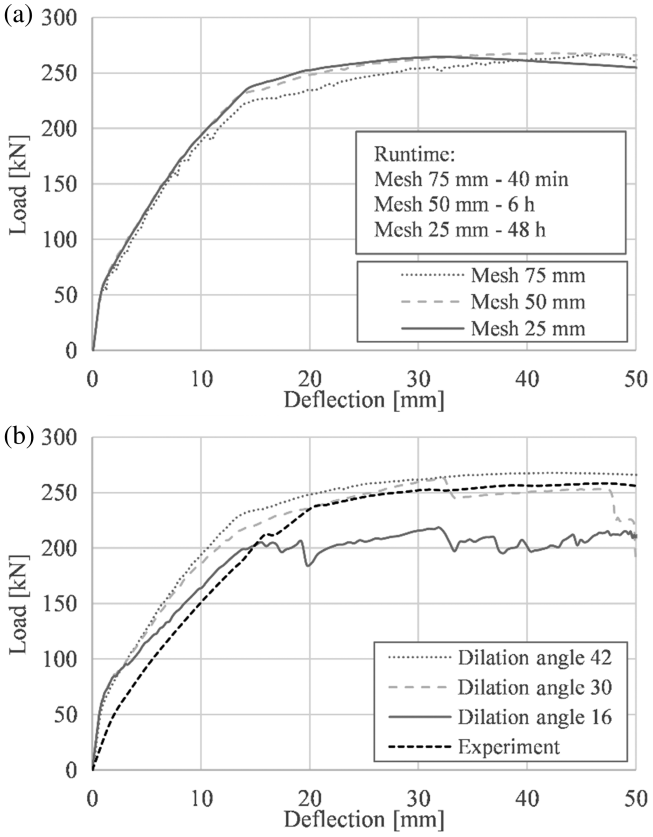

FIGURE 4 Sensitivity analysis for beam B0 (a) mesh and (b) dilation angle

applied on surfaces equal to the loading plates utilized in the actual test. Aiming at guaranteeing convergence, a quasi-static solver (Dynamic, Explicit) available in the software[41] was activated. The mesh representing the reinforcement of B0 and B30 specimens is plotted in Figure 3b. The σ–w curve for 0.38% V_f SFRC was determined by the following parameters: σ_1, σ_2, and σ_3 equal to 4.01, 0.98, and 3.01 MPa, and w_1, w_2, and w_3 equal to 0.00, 0.035, and 2.50 mm.

In order to calibrate the model, a sensitivity analysis of finite-element size and dilation angle were carried out. On the one hand, the model showed robustness in terms of the size of the element, and a 50-mm finite-element size was found suitable for the analysis in terms of runtime and preciseness (see Figure 4a). On the other hand, precaution must be taken with the dilation angle parameter, which governs the nonlinear volumetric strain of the model, set in the CDP model, especially for cases where shear failure mode can be the governing situation. In this sense, a dilation angle sensitivity analysis covering a wide range of values, from 16° up to 42°, was carried out; see Figure 4b. The curves are plotted up to 50 mm, since it was the data reported by the authors. A significant influence in the model response was found for this parameter, whereby models with values under 42° failed to reach larger values of deformation without losing load-bearing capacity. Hence, a dilation angle of 42° was chosen for this research work.

In Figure 5a,b, the load–deflection graphs for beams B0 and B30 along with the key points (cracking load, first yield, first hinge, second yield, and second hinge) are plotted, where the load corresponds to the load applied in each span. Key point values are reported in Table 2. In all cases, the first crack occurred at the intermediate support, and cracking continued for both the support and in the midspan regions of the beams up to first yield that occurred at the intermediate support; the first hinge was formed shortly before the yield at the midspan reinforcement for B0 while for B30 was produced immediately after. The final event was the formation of the second hinge in the vicinity of the midspan in the critical member. In both charts, three expected stages for this sort of tests can be clearly identified: linear behavior up to beam cracking, non-linear behavior until the second hinge was developed, which generates the collapse mechanism, and finally a horizontal trend, which ends up in collapsing. Cracking and yielding loads have been identified when tensile strength (f_{ct}) and yield strength (f_y) were reached for concrete and steel reinforcement, respectively. The sequence of the plastic hinge formation is evident from the moment–curvature diagrams (M–χ),[36] where the onset of the hinge was detected when a change in slope was spotted (see Figure 6). It is worth noticing that

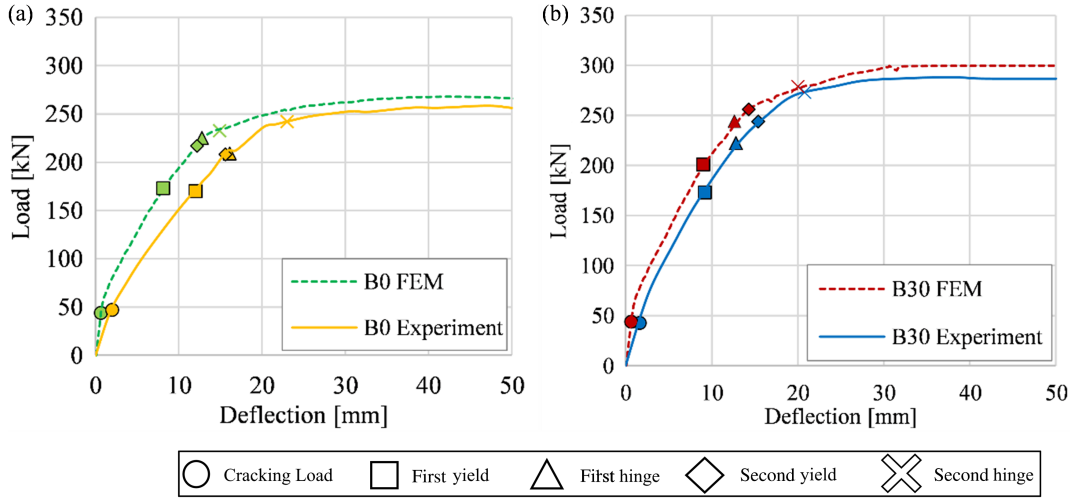

FIGURE 5 Load–deflection and key points for (a) B0 and (b) B30

TABLE 2 Key points loads for Mahmood et al.[36] beams: Experimental and numerical results

		Cracking load [kN]	First yield [kN]	First hinge [kN]	Second yield [kN]	Second hinge [kN]	Maximum load [kN]
B0	Experiment	47.2	170.0	209.0	208.0	242.0	258.0
	FEM	44.0	173.0	225.0	216.0	237.0	266.0
B30	Experiment	42.7	173.0	222.2	244.0	273.0	289.0
	FEM	44.0	201.0	244.0	256.0	279.0	299.0

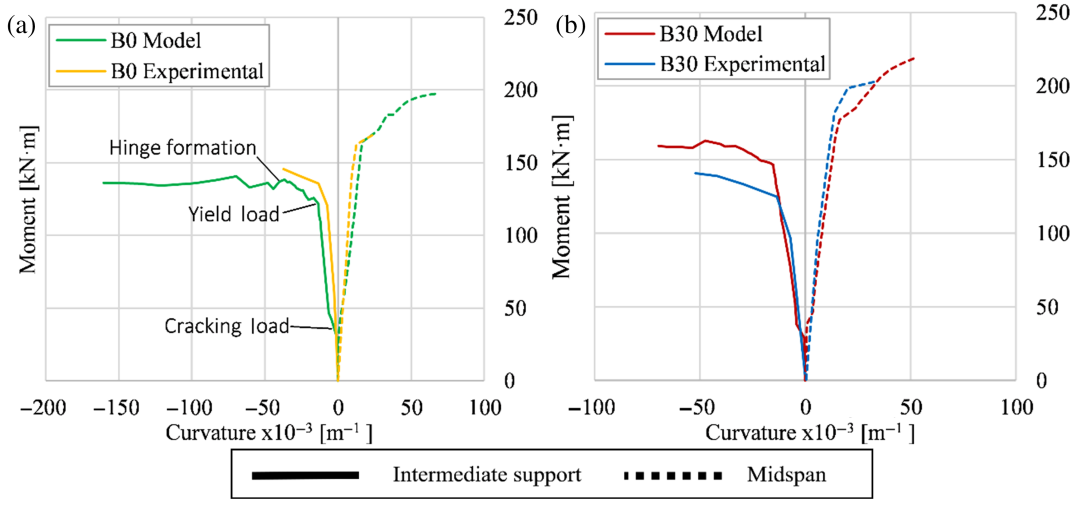

FIGURE 6 Moment–curvature for midspan and intermediate support for (a) B0 and (b) B30

cracking and yield loads can also be detected in these diagrams when a loss of stiffness (minor slope) is detected.

The graph presented in Figure 5 shows a suitable agreement between the numerical and experimental results. In case of beam B0, the key points were well captured in terms of loading; the maximum deviations found were 7.6% and 3.9% for second yield and the onset of the first hinge, respectively. For beam B30, slightly higher differences were observed for first yield (16.2%) and first hinge (9.8%), but the differences decreased for higher loading stages where the second hinge and the maximum load had a 2.2% and 3.5% of deviation, respectively. The results showed that both B0 and B30 models were able to

TABLE 3 Percentage of redistribution

		First hinge [kN]	Second yield [kN]	Second hinge [kN]	Maximum load [kN]
B0	Experimental	13.9%	14.9%	23.6%	24.7%
	Numerical model	16.2%	17.3%	24.6%	31.0%
B30	Experimental	23.7%	28.2%	32.0%	31.0%
	Numerical model	3.36%	14.0%	27.0%	29.0%

withstand the load up to over 50 mm without collapsing, showing a good rotational plastic response.

Figure 6a,b presents the M–χ diagrams; curvature was calculated as the relative difference of top and bottom strain, ε_{top} and ε_{bot}, respectively, divided by the height of the beam h (Equation (1)). ε_{top} and ε_{bot} were measured as the node relative difference of displacement, at a distance of 50 mm on either side of the centre, divided by the distance between them (100 mm).

$$\chi = \frac{\varepsilon_{bot} - \varepsilon_{top}}{h} \quad (1)$$

As it can be seen, the model results are in good agreement with the data reported in Reference 36. While for beam B0, the cracking, yield, and hinge loads were well captured, for beam B30, it can be observed that the first yield was reached at a higher moment, as reported in Table 3. Notably, higher numerical curvatures were obtained for both cases; likewise, the midspan experimental curves stopped at lower moment values; the reason for this being that in the test, the gauges were removed after reaching 24 mm of deflection for safety reasons.

Table 3 gathers the moment redistribution (K_{MR}) values for the key points after cracking. The percentage of moment redistribution was calculated as in Equation (2), where M_{el} is the theoretical elastic moment, and M_{exp} is the experimental moment that includes the contribution of the plastic behavior. The redistribution values obtained were aligned with the ones obtained by means of the experimental test reaching 30%, as per design.

$$K_{MR} = {}^{M_{el} - M_{exp}}\!/_{M_{el}} \quad (2)$$

2.3 | Model validation

2.3.1 | Moment redistribution capacity

Experimental programs carried out by Küsel and Kearsley[37] and Visintin et al.[35] were used to validate the moment redistribution modeling capacities of the calibrated FEM.

First, the study by Küsel and Kearsley[37] was used to evaluate the moment redistribution of two-span continuous beams. To this end, two-span continuous beams cast with four batches of FRC (with V_f equal to 0%, 1.01%, 1.51%, and 2.02%) combined with four tensile reinforcement arrangements (ρ_s = 0%, 0.7%, 1.4% and 2.2%) that leads to 16 beam combinations were tested. The tested beams had a clear span of 2500 mm, with a cross-sectional width and height of 200 and 220 mm, respectively. Two point loads were applied on each span, 1.0 m apart from the intermediate support. In this regard, two beams were analyzed: Beam A had V_f = 2.02% and ρ_s = 2.2%, while beam B had V_f = 1.01% and ρ_s = 1.4% (the beams are referred as 2B2.2 and 1B1.4, respectively, in Reference 37). These beams were chosen, since these had the highest and lowest V_f and fully developed the plastic mechanism and, hence, the full moment redistribution capacity. The mean compressive concrete strength (f_{cm}) was 80 MPa, and the authors provided the σ–ε tensile constitutive curves. The σ–ε data of the steel reinforcement were also provided with f_y and f_u being equal to 537 and 610 MPa, respectively, with ε_{su} equal to 0.08.

The load–deflection curves for both experimental and numerical tests along with the key points are plotted in Figure 7, and in Table 4, the data for key points are gathered.

Both models exhibited a behavior similar to that observed experimentally. The first crack and yielding were produced at the intermediate support and, subsequently, at the midspans. The key points (Table 3) show that the key points predicted by the model were in good agreement with the experimental ones, being slightly higher compared with the actual test. For beam A, the ultimate load for the numerical was the same obtained in the experimental test, whereas in Model B, the numerical test exhibited major moment redistribution from the critical section to the midspan, and therefore, this reached higher loads.

Figure 8 plots the load–moment curve for the experimental test and the numerical simulations. In Figure 8a, it can be observed that model is able to capture the

moment redistribution from the intermediate support, where the first hinge is produced, to the midspan (defined as "positive moment redistribution"). The hinges in the numerical moment were generated for higher load levels and, consequently, the redistribution started later. In case of Figure 8b, where it can be observed that the hinges appeared at the same load, the redistribution started simultaneously, and slightly more redistribution is observed in the numerical curve.

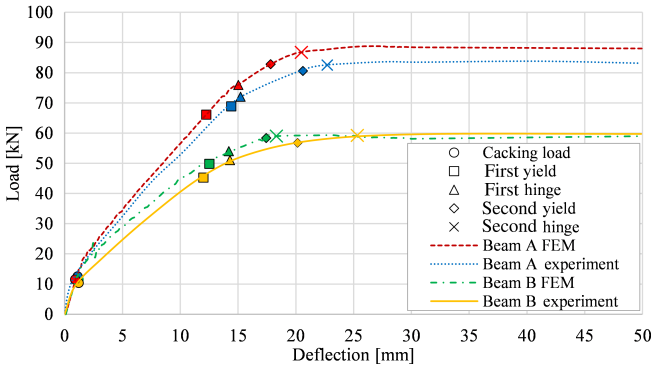

FIGURE 7 Experimental and numerical load–deflection curves for Küsel and Kearsley[37] beams A and B

The second experimental program on two-span continuous beams used for the model validation was that carried out by Visintin et al.[35] The tensile reinforcement ratio ranged from 1.13% to 1.66% in the sagging region and 0.9% to 1.66% in the hogging region, and the fiber volume fraction was 2.08% for all beams. These beams had a total length of 5500 mm length, with cross-sectional width and height of 200 and 100 mm, respectively. Point loads were located at the mid-point of each span. Direct tensile tests were conducted to determine the tensile behavior, providing the post-cracking constitutive curve ($\sigma_1 = 5.55$ MPa, $\sigma_2 = 5.27$ MPa, $\sigma_3 = 5.0$ MPa, $\sigma_4 = 3.80$ MPa and $w_1 = 0.00$ mm, $w_2 = 0.15$ mm, $w_3 = 0.40$ mm, $w_4 = 1.00$ mm), and the concrete compressive strength was 110 MPa. The σ–ε data of the steel reinforcement were also provided with f_y and f_u being equal to 580 and 610 MPa, respectively, with ε_{su} equal to 0.15.

For the model validation, 3 three-dimensional non-linear models of beams were generated: beam C ($\rho_s = 1.57\%$ at both midspan and intermediate support), beam D ($\rho_s = 1.13\%$ for the intermediate support and $\rho_s = 1.57\%$ for the midspan section), and beam E ($\rho_s = 1.57\%$ for the intermediate support and $\rho_s = 1.13\%$ for the midspan section) named as beams 1, 2, and 4 in Reference 35, respectively. With regard

TABLE 4 Key points loads for Küsel and Kearsley[37] beams: Experimental and numerical tests

		Cracking load [kN]	First yield [kN]	First hinge [kN]	Second yield [kN]	Second hinge [kN]	Ultimate load [kN]
Beam A	Experiment	12.5	68.8	72.0	80.5	83.0	83.0
	FEM	11.5	66.0	75.9	82.7	86.7	88.0
Beam B	Experiment	10.3	45.0	50.0	56.0	59.0	60.0
	FEM	11.5	49.8	54.0	58.3	59.0	59.0

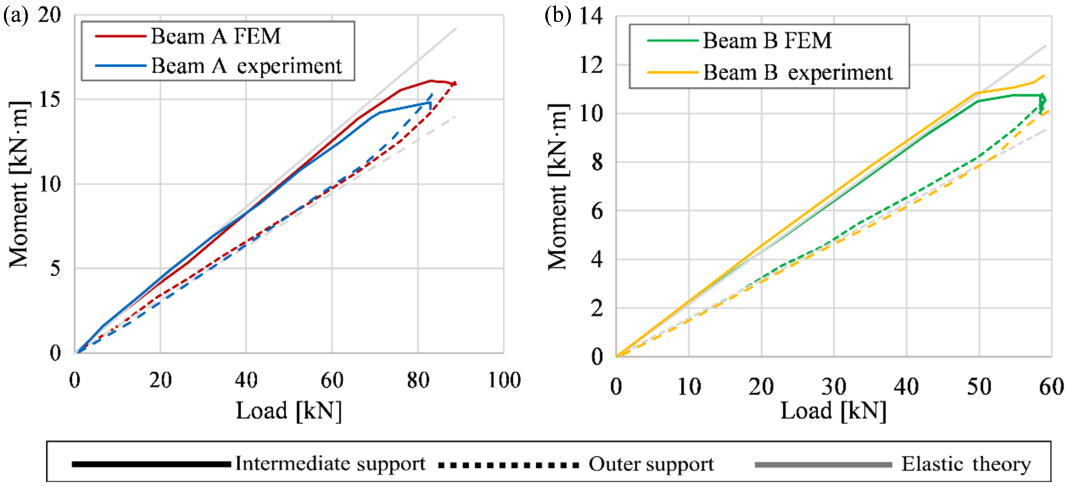

FIGURE 8 Experimental and numerical moment–load curves for (a) beam A and (b) beam B

to the reinforcement distribution, for beams C and D, positive moment redistribution was expected, whereas for beam E, the reinforcement distribution was meant to force moment redistribution from the midspan toward the intermediate support.

The load–deflection curves for both experimental and numerical tests along with the key points are plotted in Figure 9, and in Table 5, the data for key points are gathered. The results showed that the model results are in good agreement with those experimental results, and the positive (beams C and D) and negative moment redistribution (beam E) was well captured as well.

Figure 10a–c gathers the reaction-load graphs for beam C, beam D, and beam E, respectively. As it can be seen from Figure 10a,b, the redistribution from the intermediate support to midspan sections was well developed, and the FEM model for beam D captured properly the magnitude of the moment redistribution, whereas for beam C, higher redistribution was seen for the experiment, since early stages, probably, this was caused by a greater loss of stiffness after cracking. With regard to Figure 10c, the model developed the negative moment redistribution as the experimental test, although less redistribution was achieved, since the beginning, apparently due to stiffness difference.

2.3.2 | Verification of plastic hinge rotation capacity

In this section, the experimental investigation carried out by Bosco and Debernardi[39] was used for the plastic

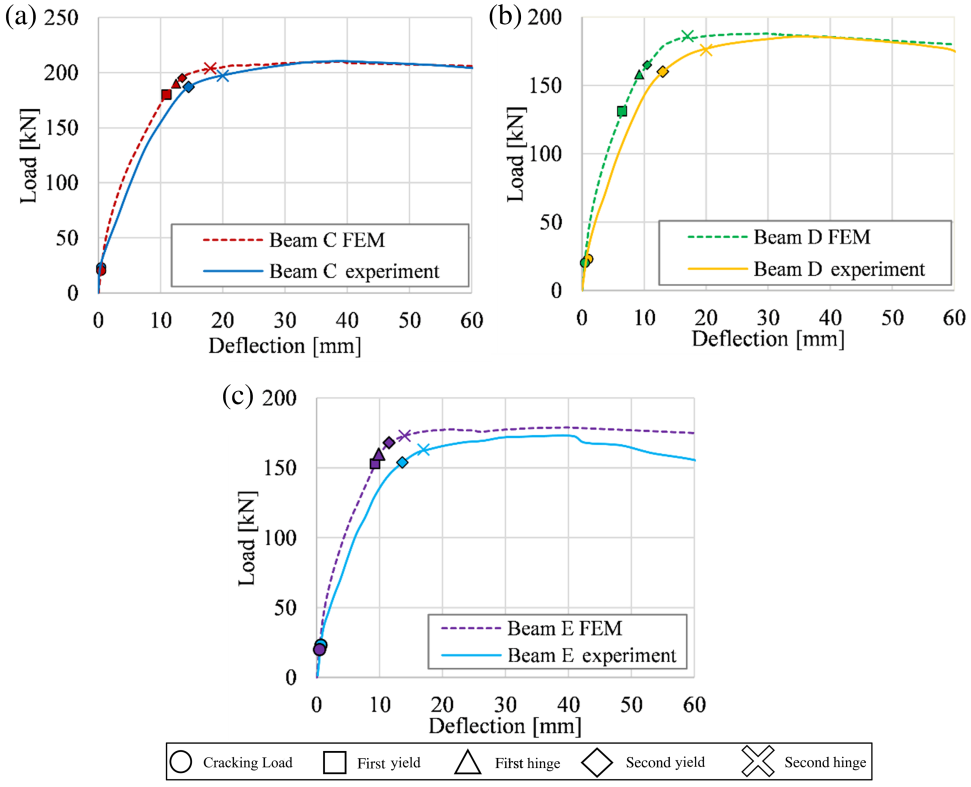

FIGURE 9 Experimental and numerical load–deflection curves for one span (a) beam C, (b) beam D, and (c) beam E from the study by Visintin et al.[35]

TABLE 5 Key points loads for Visintin et al.[35] beams: Experimental and numerical tests

		Cracking load [kN]	First yield [kN]	First hinge [kN]	Second yield [kN]	Second hinge [kN]	Ultimate load [kN]
Beam C	Experiment	28	-	-	187	209	209
	FEM	19	180	190	195	208	208
Beam D	Experiment	29	-	-	160	183	183
	FEM	19	131	140	165	187	187
Beam E	Experiment	25	-	-	154	172	172
	FEM	19	153	168	176	177	177

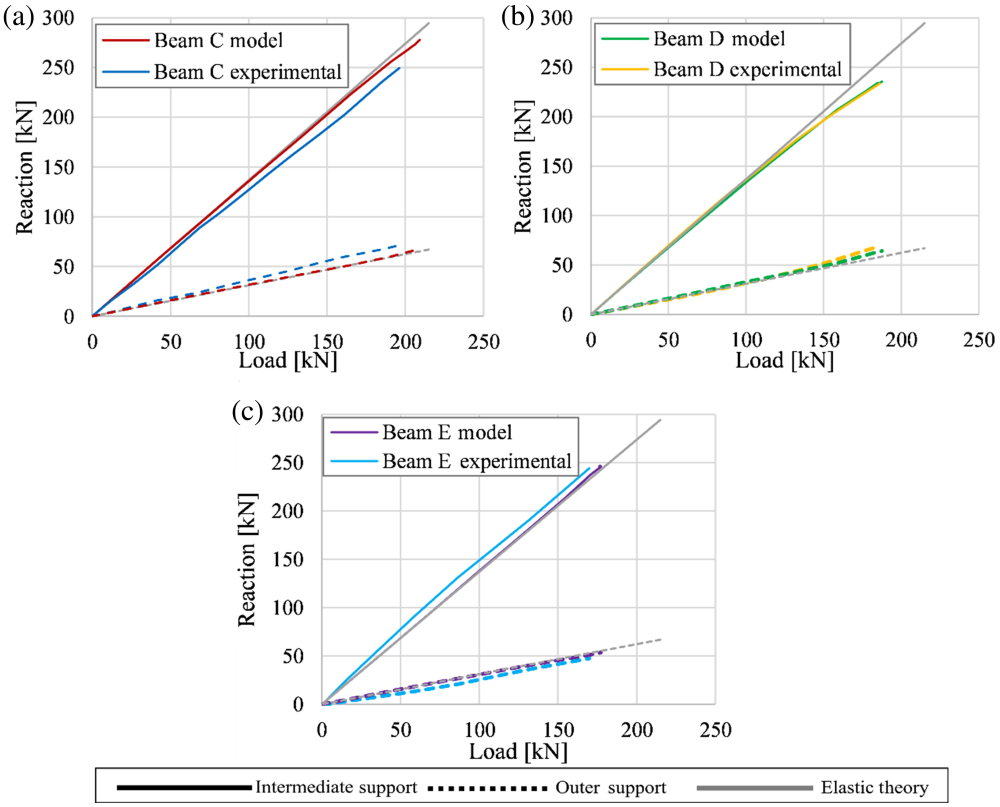

FIGURE 10 Experimental and numerical reaction–load curves for (a) beam C, (b) beam D, and (c) beam E from the study by Visintin et al.[35]

rotation capacity verification of the model. The results from these tests were also considered for other model validations.[46] For assessing the plastic rotation capacity of RC beams, a total of 44 beams were used. Different configurations were taken into account: two grades of steel ductility normal steel (grade B 500 N) and high ductility steel (grade B 500 H); three cross-sectional area were used while maintaining the same span-to-depth ratio ($L/h = 10$) and the width to depth ratio ($b/h = 1/2$), with cross-sectional depths of 200, 400, and 600 mm; the reinforcing ratios (ρ_s) varied between 0.13% and 1.14% and, finally, two different loading conditions (point load at midspan and three symmetrically arranged loads).

For the rotation capacity verification, four beams with a length of 6000 mm, cross-sectional height and width of 600 and 300 mm, respectively, (with concrete cover of 35 mm), and ρ_s of 0.13%, 0.25%, 0.57%, and 1.14% were modeled, along with Ø6 stirrups spaced every 150 mm. It is worth noticing that the rebar configuration for $\rho_s = 1.14\%$ was not provided, and an equivalent reinforcing area (6Ø20) configuration was used. All beams were reinforced with high ductility steel with $f_y = 600$ MPa, $f_u = 578$ MPa, $\varepsilon_{su} = 0.1$, and $f_{max} = 672$ MPa. Concrete had a compressive and tensile strength of 31.0 and 2.8 MPa, respectively. The analyzed beams corresponded to T8A1, T9A1, T10A1, and T11A1 in Reference 39. Hereafter, the beams are labeled with a capital S or C (for simply supported or continuous beams, introduced later within the parametric analysis) followed by a percentage (indicating ρ_s) and either RC or FRC strength class according to MC2010.[34]

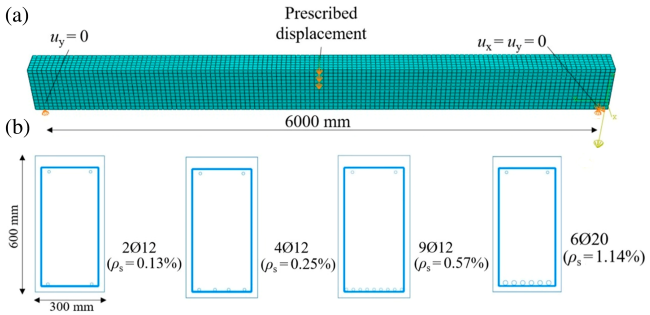

FIGURE 11 FE model (a) mesh and boundary conditions and (b) reinforcement arrangement for beams S0.13%-RC, S-0.25%-RC, and S-0.57%-RC for study[39]

Figure 11a presents the meshed model adopted for the numerical analysis and its boundary conditions: the mesh comprised 8900 50-mm C3D8R finite elements for modeling concrete, whereas the reinforcement was modeled with linear 50-mm T3D2 elements embedded in the solid elements. One support was fixed in both x and y directions ($u_x = u_y = 0$); the other was fixed only in the vertical direction ($u_y = 0$). The analyses were performed by first applying self-weight and then an increasing load

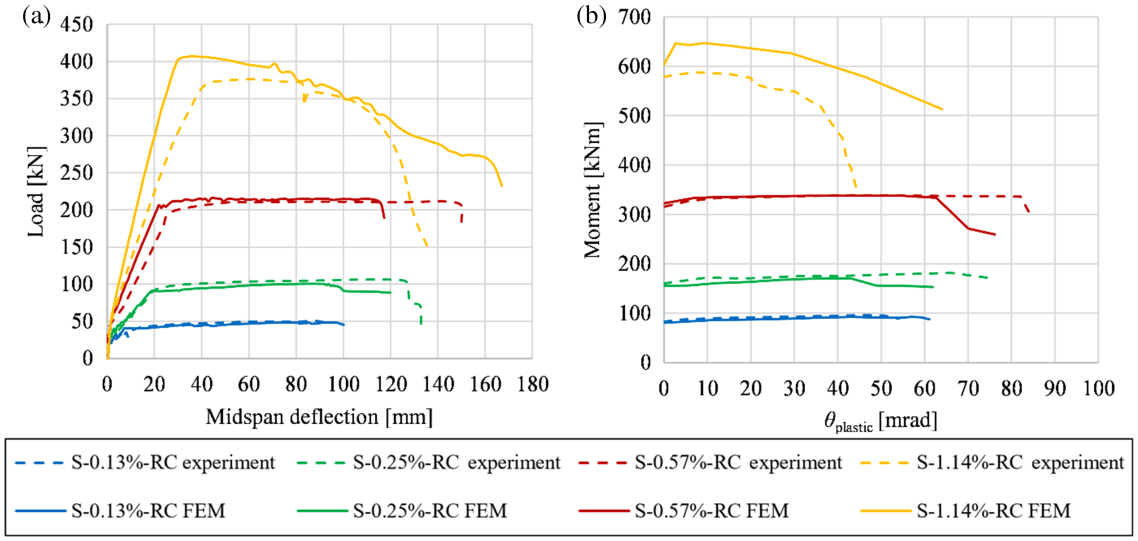

FIGURE 12 Experimental and numerical comparison of Bosco and Debernardi[39] simply supported beams (a) load–midspan deflection and (b) moment–plastic rotation

applied at the midspan by deflection control. Figure 11b shows the longitudinal reinforcement arrangement; in all cases, the compressive reinforced consisted of 2Ø12.

The comparison between the experimental and the numerical results is plotted in Figure 12a. The FEM results for the beams with $\rho_s \leq 0.57\%$ are in good agreement with the experimental in terms of load–deflection, with a slight difference in stiffness seen only in S-0.57%-RC, up to yielding loads (P_{yield}), which were well captured. These beams failed due to reinforcement failure (when the reinforcement reached ε_{su}). It was demonstrated that the model is able to simulate the plastic behavior after yielding, although major deflections were registered for beams S-0.25%-RC and S-0.57%-RC. Beam S-1.14%-RC failed due to concrete crushing, and in that case, there is a difference in stiffness and in the peak load (8.2% higher) between the model and the actual test.

Figure 12b shows the moment–plastic rotation ($\theta_{plastic}$) relationship, where the latter has been calculated by integration, along the plastic zone L_p (where the tension reinforcement had exceeded its yield limit), of the difference between the curvature (χ) and the curvature at steel yield limit (χ_y), as it is presented in Equation (3). In other words, $\theta_{plastic}$ was derived as the difference between the ultimate rotation and the rotation corresponding to the reinforcement yielding.[14,39,46] The ultimate rotation can be considered as the rotation beyond which the moment starts descending sharply according to References 47 and 48.

$$\theta_{plastic} = \int_{L_p} \left(\chi - \chi_y\right) dz \tag{3}$$

Although measuring $\theta_{plastic}$ in experimental tests can be of great difficulty due to the sudden deflection increases, the numerical results captured well the yielding moment load (M_{yield}) and the large plastic rotation, although larger rotations were registered in beams S-0.25%-RC and S-0.57%-RC. In case of concrete crushing (S-1.14%-RC), the failure mode was well captured by the model, but the plastic rotational capacity was larger than in the test. These results were found to be acceptable for the numerical model verification of beam rotational capacity to perform a parametric analysis.

3 | PARAMETRIC ANALYSES

Using the model previously calibrated and validated in Section 2, two parametrical analyses, combining different FRC strength classes and varying reinforcement ratios, were carried out. The object of this parametric analysis was to assess the influence of ρ and V_f on plastic rotation and moment redistribution capacities. The first step was to analyze the interaction between FRC flexural residual strength and HRC reinforcement ratio and its effect on plastic rotation capacity of simply supported beams. Such a choice was made as plastic rotation capacity is the prerequisite for moment redistribution in statically indeterminate structures. Then, in the second step, moment redistribution capacity was analyzed on two-span continuous beams maintaining a geometry identical to the previously analyzed simply supported beams. The beam's cross section and span length as well as the reinforcing ratio were based on the beams described in Section 2.3.2.

To this end, the reinforcement configurations of ρ_s = 0.13%, 0.25%, 0.57%, and 1.14% from the study by

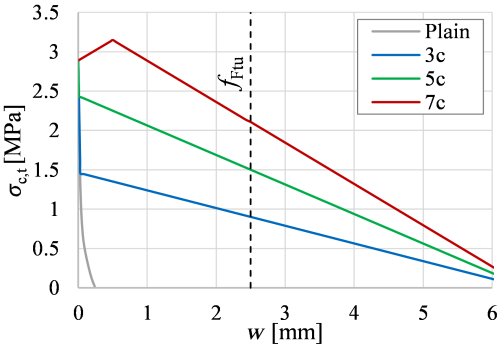

FIGURE 13 Stress crack post-cracking response of plain concrete and FRC class 3c, 5c, and 7c

Bosco and Debernardi[39] were used along with plain concrete, and three FRC mixtures were taken into account. The FRC strength classes considered, represented by f_{R1m} (mean value), were 3, 5, and 7 MPa with ductility class $f_{R3m}/f_{R1m} = 1.0$ (i.e., class "c" according to MC2010[34]). Such a ratio was chosen as being most representative of FRC structural applications (e.g., precast concrete tunnel segments according to the *fib* Bulletin 83[49]; The chosen values were considered to cover a wide range of f_R magnitudes (and indirectly, fiber contents). Furthermore, when determining the σ–w diagram according to MC2010, different post-cracking responses are obtained: FRC classes 3c and 5c exhibit a softening behavior, whereas 7c has a partially hardening behavior, Figure 13.

3.1 | Analysis of plastic rotation capacity on simply supported beams

The FEM presented in Figure 11 is used for carrying out the parametric analysis on simply supported beams. The results in terms of load–deflection and the normalized M/M_{yield}–$\theta_{plastic}/\theta_{elastic}$ relationship, up to failure, are plotted in Figure 14. In case of reinforcement failure, the failure was considered to occur at a steel deformation of $\varepsilon_{su} = 0.1$ according to MC2010,[34] and established as ULS criterion; in concrete crushing, the graphs are plotted up to a sharp load decrease. Herein, $\theta_{elastic}$ stands for the rotation achieved at the yielding limit. The results presented show that the addition of fibers affects differently to the performance of the beams depending on the reinforcing ratio. This justifying the need of carrying out this novelty parametrical analysis combining different V_f and varying reinforcing ratios.

As seen from Figure 14, for low amounts of ρ_s (i.e., 0.13% and 0.25%), a considerable enhancement of maximum load-bearing capacity caused by the addition of fibers was achieved, with the enhancement being larger for higher residual strengths. Importantly, for these beams (S-0.13% and S-0.25%), a loss of ultimate deformation capacity with the increase of V_f was also found, up to 60% for 3c FRC strength classes and 50% for the rest. As Figure 14b,d show, a softening response was produced due to the increase of V_f after reaching the reinforcement yielding. The results obtained are aligned with the behavior observed in actual beam tests conducted by and reported in References 8–12.

For $\rho_s = 0.57\%$, the addition of fibers also led to an increase in load-bearing capacity but did not produce a softening post-yielding response. In this case, a lower FRC residual strength (beam S-0.57%-3c) resulted in a slight increase of deformation capacity, 6%, although the onset of crack localization was detected in the model. However, the influence of this crack localization became more evident in the performance of beams S-0.57%-5c and S-0.57%-7c, which suffered a reduction in deformation capacity, 42% and 30%, respectively, reaching a significantly lower ultimate deflection than beam S-0.57%-RC. Crack localization was detected in the model, since as the load progressively increased, a few cracks became wider and predominant over the rest. In beams with $\rho_s = 1.14\%$, only a slight increase of the ultimate load was found with the increment of f_{R1}, and the governing mode of failure of the beams was concrete crushing for all cases. Crack localization was also detected for high V_f resulting in a reduction of ultimate deflection capacity, 40% and 30% for S-1.14%-5c and S-1.14%-7c, respectively.

According to the presented results, to develop the full plastic rotation mechanism of HRC members, characterized by a plateau in the load–deflection relationship after yielding, reinforcement ratios of at least 0.3%–0.5% are required. The results of the study demonstrate that for $\rho_s = 0.57\%$, full rotation capacity is already achieved. However, since crack localization is detected for class 5c and 7c and not for 3c, it is probable that the "minimum reinforcement ratio" for ductility decreases with increasing residual strength class (i.e., it is ~0.5% for 3c but likely lower for 5c and lower still for 7c).

For higher amounts of reinforcement (i.e., $\rho_s = 1.14\%$), the failure mode turns from reinforcement failure to concrete crushing, disabling the development of such ductile failure mechanisms.

In order to quantitatively quantifying the ductility degree of the beams, a ductility index (μ) was adopted, defined by Equation (4), where δ_u stands for the ultimate deflection capacity and δ_y the deflection at rebar yielding.

$$\mu = \frac{\delta_u}{\delta_y} \tag{4}$$

For any reinforcement ratio, see Figure 15, there was a ductility reduction with the increase of V_f, and the results

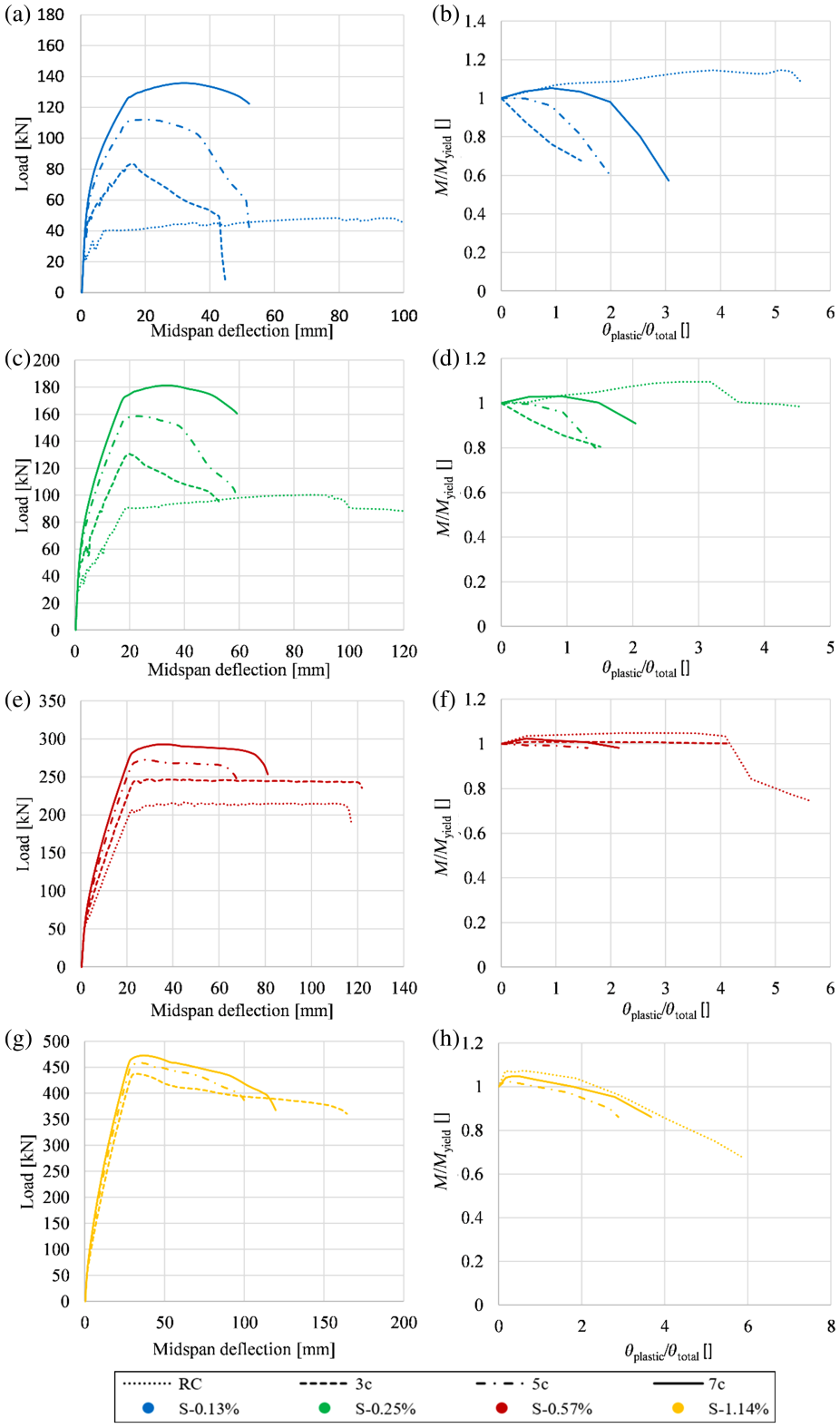

FIGURE 14 Parametrical analysis on simply supported beams: Load–deflection and M/M_{yield}–$\theta_{plastic}/\theta_{total}$

were aligned with those obtained in previous studies.[8,9] However, whereas the authors of previous studies found that the lowest ductility was expected for low ρ_s and high V_f, the results presented in Figure 15 showed that the lowest values of μ are found for low ρ_s (0.13% and 0.25%) and low V_f (this being a direct proxy for residual strength), with μ increasing with increasing V_f. For beams S-0.57% and S-1.14%, μ is higher for low amounts of fibers; as explained earlier, this behavior was caused by crack localization.

Finally, Figure 16a represents the ultimate plastic rotation $\theta_{plastic\_u}$–f_{R1} relationship. It can be seen that for higher

residual strength classes (5c and 7c), $\theta_{plastic\_u}$ is less sensitive to ρ_s than for class 3c. Namely, for class 3c, $\theta_{plastic\_u}$ increases almost five times when increasing ρ_s from 0.13% and 0.25% to 1.14%, whereas for classes 5c and 7c, this increase is only around 2.5 times, that is, twice smaller. In other words, changes in longitudinal reinforcement have a much larger effect (in terms of both load-bearing capacity and ductility degree) for lower FRC residual strength classes. This is of particular importance when FRC is used as a way of reducing the longitudinal reinforcement ratio.

Figure 16b shows the relation between the plastic hinge length L_p (detected as the length along which the yield strain in steel is exceeded) and FRC residual strength. The figure demonstrates that L_p remained slightly affected by the increase of f_{Rm} for $\rho_s = 0.57\%$ and $\rho_s = 1.14\%$ but was remarkably affected for low ρ_s: for these beams, L_p decreases with decreasing FRC residual strength. These results are aligned with the conclusion obtained with regards to deformation capacity and post-yield response, discussed earlier.

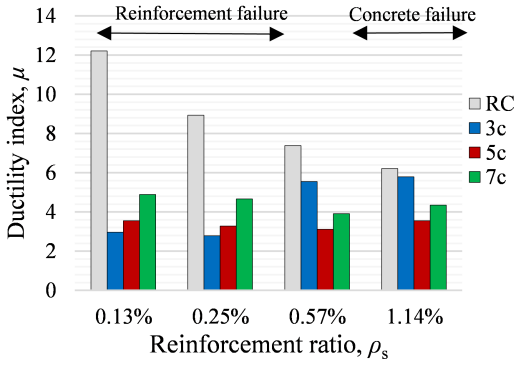

FIGURE 15 Ductility of simply supported beams

3.2 | Analysis of moment redistribution capacity on two-span continuous beams

After analyzing the plastic rotation capacity of HRC beams in the first parametric analysis, a second one was performed to assess the effects of changes in plastic rotation capacity on moment redistribution in statically indeterminate HRC beams. Based on the geometry of the beams presented in Sections 2.3.2 and 3.1 (clear span of 6000 mm, and depth and width of 600 and 300 mm, respectively), two-span continuous beams were considered in the analysis. The reinforcement configurations were again $\rho_s = 0.13\%$, 0.25%, 0.57%, and 1.14% along with plain concrete and three FRC mixtures ($f_{R1m} = f_{R3m}$ equal to 3, 5, and 7 MPa). Compressive longitudinal reinforcement consisted of 2Ø12, and transversal reinforcement consisted of Ø6 spaced at 150 mm, except for $\rho_s = 1.14\%$ in which stirrups were Ø8 at a spacing of 150 mm, for reasons of shear.

Figure 17a presents the meshed model, its geometry and boundary conditions: one support was fixed in both x and y directions of translational degrees of freedom ($u_x = u_y = 0$), and the rest were fixed only in the vertical direction ($u_y = 0$). The mesh was comprised of 17,600 50-mm C3D8R finite elements for concrete, and the reinforcement was modeled with linear 50-mm T3D2 finite elements embedded in the solid elements. Figure 17b–e presents the reinforced models: the length of tensile longitudinal reinforcement for sagging and hogging regions was 1.1 times the theoretical elastic length, which led to an overlap length of 0.8 m. The analysis was performed by first applying self-weight, and subsequently, two-point loads were applied at both midspans. Considering the applied longitudinal reinforcement arrangement, moment redistribution was expected from the hogging to sagging regions (from the intermediate support to the midspan section).

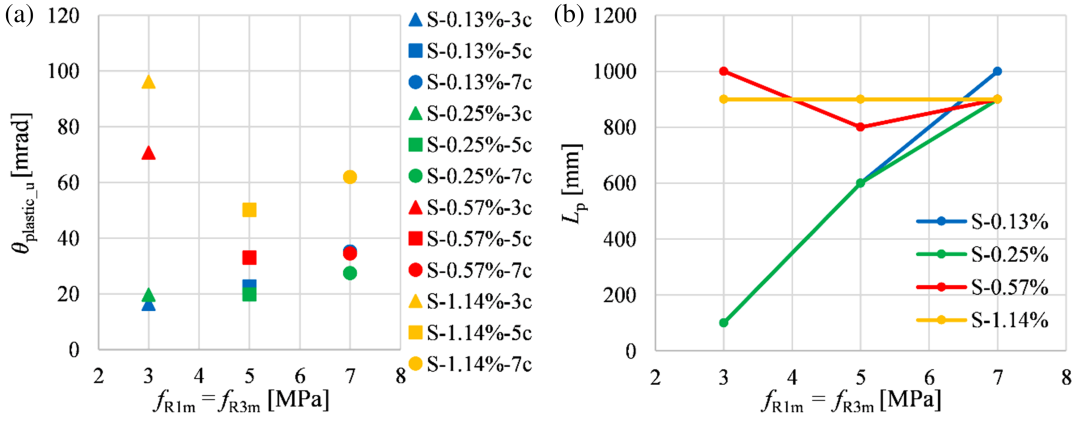

FIGURE 16 Results based on residual strength (a) $\theta_{plastic\_u}$ and (b) L_p

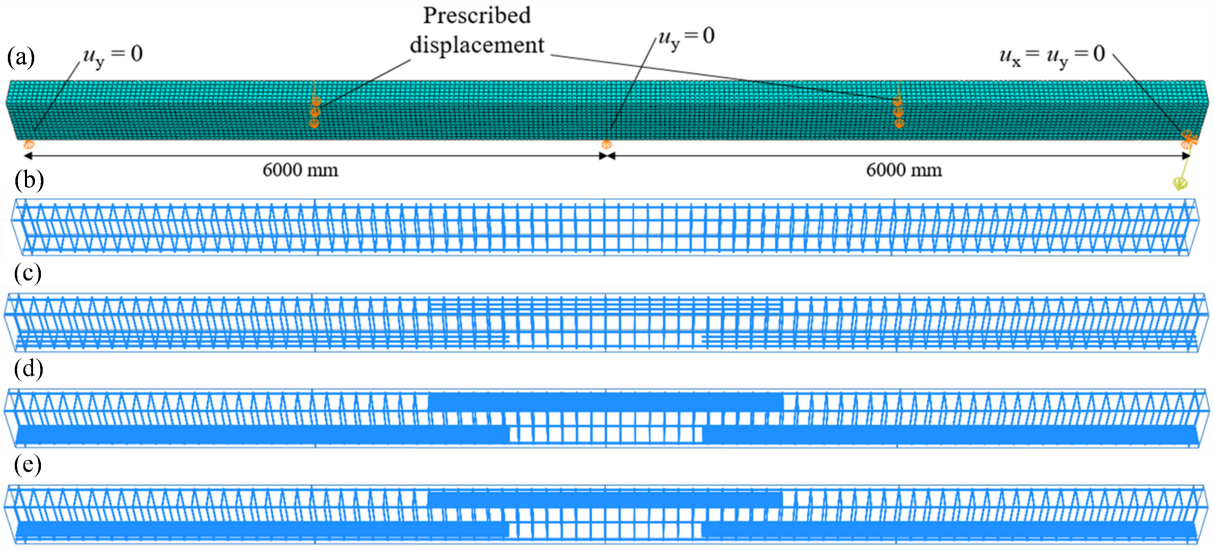

FIGURE 17 FEM (a) mesh and boundary conditions and (b) reinforcement arrangement for beams C-0.13%, (c) reinforcement arrangement for beams C-0.25%, (d) reinforcement arrangement for beams C-0.57%, and (e) reinforcement arrangement for beams C-1.14%

The results are presented in Figure 18 in terms of load–midspan deflection and M/M_{yield}–$\theta_{plastic}/\theta_{elastic}$ (at the intermediate support) relationships, up to reinforcement failure (ε_s = 10‰), with the plastic rotation calculated according to Equation (1). As expected, the first cracking occurred at the intermediate support and subsequently in the midspan section, in all cases studied. The increase of f_{R1} affected the overall response of the statically indeterminate members in different ways depending on ρ_s. For ρ_s = 0.13%, the addition of fibers resulted in an increase of the load-bearing capacity and enhancing the ultimate deflection capacity. Contrary to the results presented in Figure 14a for simply supported beams, the increase of f_{R1} did not reduce the deflection capacity of the beam but enhanced it. However, as it can be seen in Figure 18b, the use of HRC led to a softening response after yielding at the intermediate support (except for C-0.13%-7c where hardening was appreciated at the onset due to its post-cracking response, followed by softening) while C-0.13%-RC presented a hardening response.

In case of ρ_s = 0.25% (Figure 18c,d), the use of HRC enhanced the load-bearing capacity and the overall stiffness. Similar to the response of simply supported beams with ρ_s = 0.25%, the enhancement of the load-bearing capacity for the solutions with fibers was in detriment of the deformation capacity, which was significantly reduced. As for C-0.13%, C-0.25%-3c and 5c presented a softening response after reinforcement yielding; for C-0.25%-7c, a slight hardening was registered before softening, and for C-0.25%-RC, deflection hardening with associated ductility was detected.

For simply supported beams with ρ_s = 0.57%, an increase of the load-bearing capacity was found and even an enhanced deformation capacity in case of FRC concrete class 3c. In all cases, a ductile response was produced after yielding. In contrast, for continuous beams C-0.57% (Figure 18e,f), combining steel reinforcement and fibers only led to a load-bearing capacity and stiffness enhancement, and a clear loss of deformation capacity was observed along with a softening behavior after reaching the reinforcement yield. For the highest amount of reinforcement studied of ρ_s = 1.14%, Figure 18g,h, the failure of the beams was due to concrete crushing at the mid-support. In C-1.14%-RC, the beam failed prior to reinforcement yield, and the use of fibers enhanced the load-bearing capacity of the beams and significantly increased (100% in all cases) the deformation capacity of the conventional solution, improving the ductility before failure.

The moment redistribution capacity was computed using the K_{MR} coefficient (see Equation (2)). Then, the coefficient K_{MR} was plotted against $\theta_{plastic}$ and presented in Figure 19, with both K_{MR} and $\theta_{plastic}$ measured at the intermediate support. As the coefficient K_{MR} quantifies the capacity of transferring forces from critical sections toward those less demanded, the graphs depicted in Figure 19 are presented up to the point when loads started decreasing. For low amounts of reinforcement (0.13% and 0.25%), it can clearly be seen that at the onset of yielding a bigger redistribution of moments had already been produced for the RC configurations compared with those HRC beams, due to the loss of stiffness after the section cracking. This is aligned with the behavior shown in Figure 18a,c. For C-0.13%

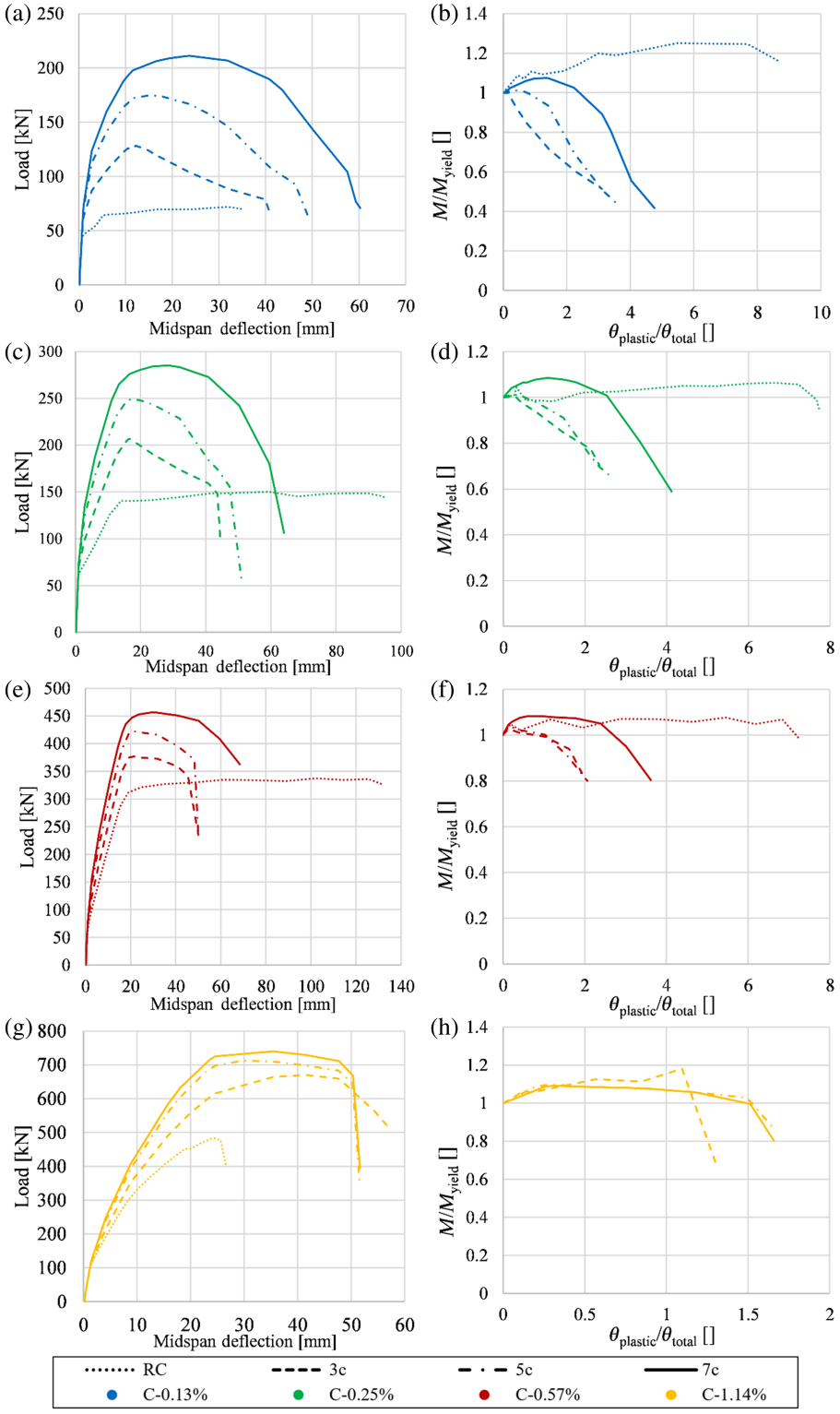

FIGURE 18 Parametrical analysis on two-span continuous beams: Load–deflection and M/M_{yield}–$\theta_{plastic}/\theta_{total}$

beams, the solutions with fibers presented lower plastic rotations compared to C-0.13%-RC. In case of $\rho_s = 0.25\%$, the stiffness after yielding was similar meaning that the addition of fibers for this reinforcement configuration had less impact on the post-yielding stiffness. Again, the RC configuration achieved larger plastic deformations. For $\rho_s = 0.57\%$, K_{MR} at rebar yielding was similar in all cases; for this amount of longitudinal reinforcement, the addition of fibers barely affected the loss of stiffness after cracking. After yielding, the K_{MR}–$\theta_{plastic}$ curves had the same slope, C-0.52%-RC being the unique solution able to present high plastic rotation capacity. In case of $\rho_s = 1.14\%$, all beams had similar redistribution at the onset of rebar yielding, so the increase of f_{R1} unaltered the overall stiffness of the

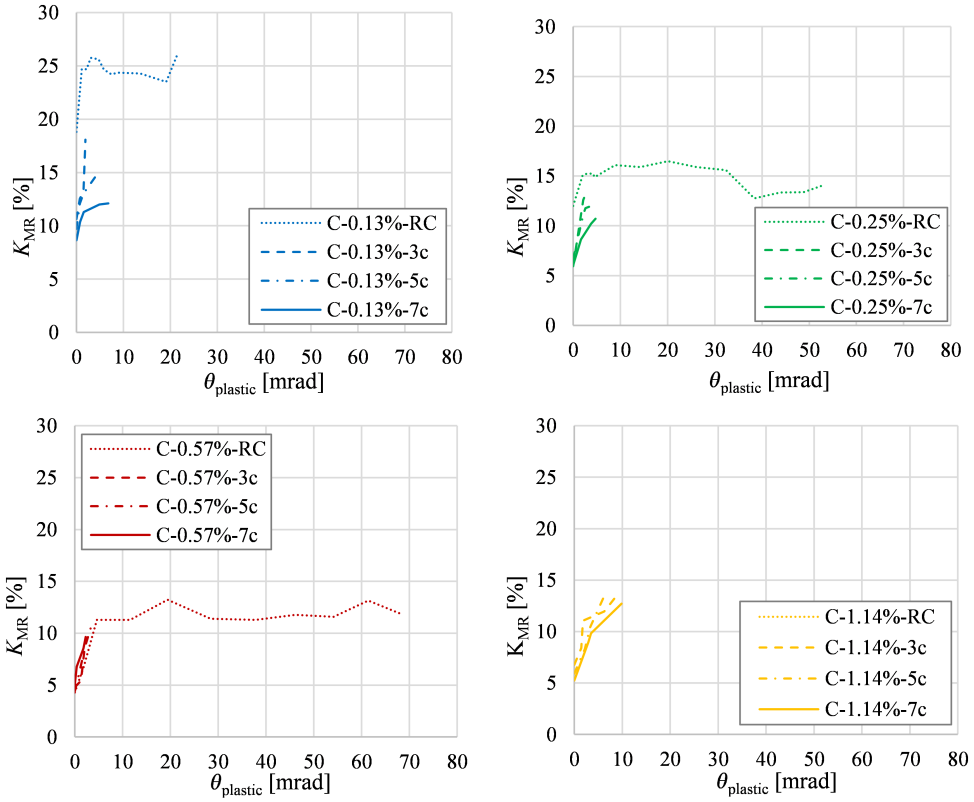

FIGURE 19 Parametrical analysis on two-span continuous beams: K_{MR}–$\theta_{plastic}$ graphs for (a) C-0.13%, (b) C-0.25%, (c) C-0.57%, and (d) C-0.1.14%

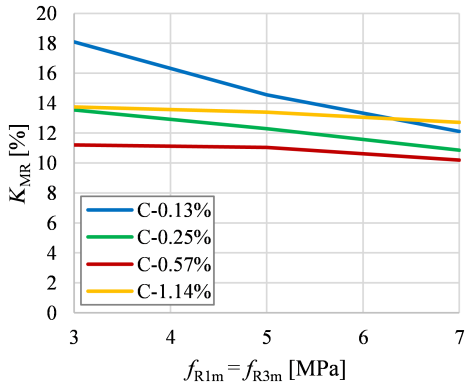

FIGURE 20 K_{MR}–f_{R1m} relationship for two-span continuous beams

member, and the same range of moment redistribution was detected, ranging from 11% to 13%.

Finally, Figure 20 presents the K_{MR}–f_{R1m} relationship. First, for reinforcement ratios higher than 0.57%, K_{MR} ranges between 10% and 14%, this being barely affected by FRC residual strength (although it remains significantly lower than for the RC solution). As reinforcement ratio decreases to 0.25% and 0.13%, K_{MR} becomes increasingly sensitive to f_{R1m}, particularly for a reinforcement ratio of 0.13% for which it linearly decreases with increasing f_{R1m}.

In the light of the previous results, it must be emphasized that the redistribution capacity of 20% accepted in the *fib* MC2010 (or even higher in other codes) for FRC structural members should be revised, especially in case of low longitudinal reinforcement ratios.

4 | CONCLUSIONS

This paper has presented the results of a numerical parametric study on the plastic rotation and moment redistribution capacities in HRC members with different reinforcing ratios (from 0.13% to 1.14%) and FRC residual strengths (classes 3c, 5c, and 7c per MC2010[34]). Plastic rotation capacity was assessed on simply supported beams, whereas two-span continuous beams were used to analyze the moment redistribution capacity. For this purpose, a numerical model was developed and validated on experimental data. The simulations were carried out using high ductility reinforcement (f_{max}/f_y = 672/600); therefore, the conclusions drawn in this paper only can be hold when this class of steel is used.

Based on the obtained results, the following conclusions can be drawn:

- The increase of the FRC strength class (represented by f_{R1}) in both simply supported and continuous beams led to increases in load-bearing capacity, especially for low values of ρ_s.
- The use of fibers in simply supported beams significantly affected the deformation capacity of those by reducing

both deformation and rotation capacities for any FRC residual strength class in beams with $\rho_s \leq 0.25\%$.

- In simply supported beams with $\rho_s = 0.57\%$, there was an increase in deformation capacity due to the interaction of the softening response of FRC residual strength class 3c and the hardening of the steel reinforcement. For the remaining values of FRC residual strength classes (5c and 7c), crack localization affected the deformation capacity leading to a clear reduction of this property. For HRC beams with $\rho_s = 1.14\%$, the beams failed due to concrete crushing, and crack localization was also detected; hence, a reduction of deformation capacity was found for all beams.
- In simply supported beams, changes in ρ_s have higher influence on the rotational capacity for lower FRC residual classes (3c) than for those with higher FRC classes. For $\rho_s \leq 0.57\%$, the plastic hinge length is not affected by the addition of fibers, whereas for lower ratios, the length decreases with the decrease of the FRC residual strength.
- In statically indeterminate members, prior to yielding, the increase of f_{R1} reduces the moment redistribution by enhancing the overall stiffness. As expected and in agreement with results from the literature, the addition of fibers increased the load-bearing capacity, with the contribution increasing when decreasing ρ_s.
- In HRC continuous beams, the deformation capacity only improved for beams with $\rho_s = 1.14\%$. For the rest of beams, a reduction of the post-yield ductility response of the beam was observed.
- The moment redistribution capacity was not affected by the FRC residual strength for beams with $\rho_s \geq 0.57\%$. For low reinforcement ratios (i.e., 0.13% and 0.25%), the redistribution capacity became more sensitive; this increases with decreasing f_{R1}.
- The latter conclusion is of paramount importance, since the redistribution coefficient accepted in several design guidelines (including the *fib* MC2010) is superior to 20%. The results obtained numerically prove that lower redistribution coefficients are to be expected when the FRC strength class increases in HRC when those are compared with the equivalent (same reinforcement ratio) RC alternative.

The conclusions of this study are determined by the ranges of parameter values considered in the analyses and, therefore, cannot be directly extrapolated beyond these values. Although the numerical model was calibrated and validated on experiments using steel FRC, it can be considered that, in general, the results are applicable also to FRC produced with macro-synthetic structural fibers as long as requirements of subclause 5.6.1 of the *fib* Model Code 2010 are fulfilled. Therefore, the results of this study can serve as an important first step toward defining moment redistribution and rotation capacity models and limits for HRC. Future studies should include more experimental tests, ranges of FRC residual strengths, as well as different statical systems and load distributions.

ACKNOWLEDGMENTS

The authors express their gratitude to the Spanish Ministry of Economy, Industry and Competitiveness for the financial support received under the scope of the project CREEF (PID2019-108978RB-C32). Likewise, the first author acknowledges the Spanish Ministry of Science, Innovation and University for providing support through the PhD Industrial Fellowship (DI-17-09390) in collaboration with Smart Engineering Ltd. (UPC's Spin-Off).

NOTATION

List of symbols

CMOD	crack mouth opening displacement
E_c	modulus of elasticity for concrete
E_{ci}	tangent modulus of elasticity of concrete at a stress σ_i
E_{c1}	secant modulus from the origin to the peak compressive stress
f_c	mean value of the cylindrical compressive concrete
f_{ct}	tensile concrete strength
f_{Fts}	serviceability residual strength (post-cracking strength for serviceability crack opening)
f_{Ftu}	ultimate residual strength (post-cracking strength for ultimate crack opening)
$f_{R,j}$	value of the residual flexural strength corresponding to CMOD = CMODj
f_y	yield strength of steel reinforcement
f_u	ultimate strength of steel reinforcement
f_{max}	maximum strength of steel reinforcement
G_F	fracture energy of concrete
h	beam height
KMR	moment redistribution ratio
M_{el}	theoretical elastic moment
M_{exp}	moment measured experimentally
V_f	fiber volume fraction
w	crack opening in mm
w_s	crack opening for f_{Fts}
w_t	crack opening when $\sigma_j = 0$
w_u	crack opening for f_{Ftu}
ε_1	concrete strain for f_{ctm}
ε_c	concrete compression strain
ε_{bottom}	strain at the bottom layer of the beam
ε_{top}	strain at the top layer of the beam
ρ_s	longitudinal reinforcement ratio
σ_c	concrete compression stress
σ_j	stress point for concrete tensile constitutive curve, j being the point numbering

$\theta_{elastic}$ plastic rotation
$\theta_{plastic}$ elastic rotation
χ curvature
χ_y curvature at steel yield strength

DATA AVAILABILITY STATEMENT

Data sharing not applicable to this article as no datasets were generated or analysed during the current study

ORCID

Alejandro Nogales https://orcid.org/0000-0002-7009-8440
Nikola Tošić https://orcid.org/0000-0003-0242-8804
Albert de la Fuente https://orcid.org/0000-0002-8016-1677

REFERENCES

1. Conforti A, Minelli F, Plizzari GA. Wide-shallow beams with and without steel fibres: a peculiar behaviour in shear and flexure. Compos Part B Eng. 2013;51:282–90. https://doi.org/10.1016/j.compositesb.2013.03.033
2. Meda A, Minelli F, Plizzari GA. Flexural behaviour of RC beams in fibre reinforced concrete. Compos Part B Eng. 2012;43(8):2930–7. https://doi.org/10.1016/j.compositesb.2012.06.003
3. Pfyl T, Marti P Behaviour of reinforced steel fibre concrete members in bending and tensions. In *Proceedings of the 3rd International PhD Symposium in Civil Engineering* (Vol. 2, pp. 47–55). 2000.
4. Pujadas P, Blanco A, de la Fuente A, Aguado A. Cracking behavior of FRC slabs with traditional reinforcement. Mater Struct. 2012;45(5):707–25. https://doi.org/10.1617/s11527-011-9791-0
5. Fantilli AP, Chiaia B, Gorino A. Unified approach for minimum reinforcement of concrete beams. ACI Struct J. 2016a;113(5):1107–16. https://doi.org/10.14359/51688927
6. Fantilli AP, Gorino A, Chiaia B. Fiber volume fraction and ductility index in fiber-reinforced concrete round determined panels. Procedia Struct Integr. 2016b;2:2857–64. https://doi.org/10.1016/j.prostr.2016.06.357
7. Markić T, Amin A, Kaufmann W, Pfyl T. Strength and deformation capacity of tension and flexural RC members containing steel fibers. J Struct Eng (United States). 2020;146(5):1–17. https://doi.org/10.1061/(ASCE)ST.1943-541X.0002614
8. Yoo DY, Moon DY. Effect of steel fibers on the flexural behavior of RC beams with very low reinforcement ratios. Constr Build Mater. 2018;188:237–54. https://doi.org/10.1016/j.conbuildmat.2018.08.099
9. Dancygier AN, Berkover E. Cracking localization and reduced ductility in fiber-reinforced concrete beams with low reinforcement ratios. Eng Struct. 2016;111:411–24. https://doi.org/10.1016/j.engstruct.2015.11.046
10. Dancygier AN, Savir Z. Flexural behavior of HSFRC with low reinforcement ratios. Eng Struct. 2006;28(11):1503–12. https://doi.org/10.1016/j.engstruct.2006.02.005
11. Espion B. Discussion of 'Flexural analysis of reinforced concrete beams containing steel fibers' by Byung Hwan Oh (October, 1992, Vol. 118, No. 10). Struct Eng. 1994;120((6)):1932–4. https://doi.org/10.1061/(ASCE)0733-9445(1994)120:6(1932)
12. Mertol HC, Baran E, Bello HJ. Flexural behavior of lightly and heavily reinforced steel fiber concrete beams. Constr Build Mater. 2015;98:185–93. https://doi.org/10.1016/j.conbuildmat.2015.08.032
13. Conforti A, Zerbino R, Plizzari G. Assessing the influence of fibers on the flexural behavior of reinforced concrete beams with different longitudinal reinforcement ratios. Struct Concr. 2020(22):347–360. https://doi.org/10.1002/suco.201900575
14. Pokhrel M, Shao Y, Billington S, Bandelt MJ. Effect of Fiber Content Variation in Plastic Hinge Region of Reinforced UHPC Flexural Members. In BEFIB 2020 (Vol. 30, pp. 1042–1055). https://doi.org/10.1007/978-3-030-58482-5_92
15. Meda A, Plizzari G. New design approach for steel fiber-reinforced concrete slabs-on-ground based on fracture mechanics. ACI Struct J. 2004;101(3):298–303.
16. Meda A, Plizzari GA, Riva P. Fracture behavior of SFRC slabs on grade. Mater Struct. 2004;37(270):405–11. https://doi.org/10.1617/14093
17. de la Fuente A, Pujadas P, Blanco A, Aguado A. Experiences in Barcelona with the use of fibres in segmental linings. Tunn Undergr Space Technol. 2012b;27(1):60–71. https://doi.org/10.1016/j.tust.2011.07.001
18. de la Fuente A, Escariz RC, de Figueiredo AD, Aguado A. Design of macro-synthetic fibre reinforced concrete pipes. Constr Build Mater. 2013;43:523–32. https://doi.org/10.1016/j.conbuildmat.2013.02.036
19. de la Fuente A, Escariz RC, de Figueiredo AD, Molins C, Aguado A. A new design method for steel fibre reinforced concrete pipes. Constr Build Mater. 2012a;30:547–55. https://doi.org/10.1016/j.conbuildmat.2011.12.015
20. Paulay T. Moment redistribution in continuous beam of earthquake resistan multistory reinforced concrete frames. Bulletin of the New Zealand Society for Earthquake Engineering, 9(4), 205–212. 1976. Retrieved from: https://doi.org/10.5459/bnzsee.9.4.205-212
21. Visintin P, Oehlers DJ. Mechanics-based closed-form solutions for moment redistribution in RC beams. Struct Concr. 2016;17(3):377–89. https://doi.org/10.1002/suco.201500085
22. Scott RH, Whittle RT. Moment redistribution effects in beams. Mag Concr Res. 2005a;57:9–20.
23. Nethercot DA, Li TQ, Choo BS. Required rotations and moment redistribution for composite frames and continuous beams. J Constr Steel Res. 1995;35:121–63.
24. Oehlers DJ, Haskett M, Mohamad Ali MS, Griffith MC. Moment redistribution in reinforced concrete beams. Struct Build. 2010;163:165–76.
25. Oehlers DJ, Ju G, Liu IST, Seracino R. Moment redistribution in continuous plated RC flexural members. Part1: netral axis depth approach and tests. Eng Struct. 2004a;26:2197–207.
26. Oehlers DJ, Liu IST, Ju G, Seracino R. Moment redistribution in continuous plated RC flexural members. Part2: flexural rigidity approach. Eng Struct. 2004b;26:2209–18.
27. Scott RH, Whittle RT. Serviceability influences on moment redistribution in beams. Struct Concr. 2005b;6(4):135–40. https://doi.org/10.1680/stco.2005.6.4.135
28. Lou T, Lopes SMR, Lopes AV. Effect of relative stiffness on moment redistribution in reinforced high-strength concrete beams. Mag Concr Res. 2017;69(14):716–27. https://doi.org/10.1680/jmacr.15.00499

29. Sturm AB, Visintin P, Oehlers DJ. Closed-form expressions for predicting moment redistribution in reinforced concrete beams with application to conventional concrete and ultrahigh performance fiber reinforced concrete. Struct Concr. 2020;21(4):1577–96. https://doi.org/10.1002/suco.201900498
30. 318-08, A. ACI Committee, American Concrete Institut and International Organization for Standaritzation, Building Code Requirements for Structural Concrete. Farmington Hills: ACI. 2008.
31. AS 360 - 2009. AS 3600-2009 Concrete Structures. Australian Standards. 2009.
32. EHE-08. Instrucción de Hormigón Estructrural (EHE-08). Madrid: Ministerio de Fomento. 2008. Retrieved from: http://www.aigcm.es/awback/app/webroot/img/bibliotecas/ehe2008.pdf
33. EN 1992-1-1:2011-01. Eurocode 2. Brussels: CEN. (2014). https://doi.org/10.2788/35386
34. International Federation for Structural Concrete (fib). Fib model code for concrete structures 2010. Lausanne, Switzerland; fédération internationale du béton / International Federation for Structural Concrete (fib); 2010. https://doi.org/10.1002/9783433604090
35. Visintin P, Mohamad Ali MS, Xie T, Sturm AB. Experimental investigation of moment redistribution in ultra-high performance fibre reinforced concrete beams. Constr Build Mater. 2018;166:433–44. https://doi.org/10.1016/j.conbuildmat.2018.01.156
36. Mahmood SMF, Agarwal A, Foster SJ, Valipour H. Flexural performance of steel fibre reinforced concrete beams designed for moment redistribution. Eng Struct. 2018;177((October)):695–706. https://doi.org/10.1016/j.engstruct.2018.10.007
37. Küsel F, Kearsley E. Effect of steel fibres in combination with different reinforcing ratios on the performance of continuous beams. Constr Build Mater. 2019;227:116553. https://doi.org/10.1016/j.conbuildmat.2019.07.279
38. Markić T, Amin A, Kaufmann W, Pfyl T. Discussion on "Assessing the influence of fibers on the flexural behavior of reinforced concrete beams with different longitudinal reinforcement ratios" by Conforti et al. [structural concrete, 2020]. Struct Concr. 2021;22(5). https://doi.org/10.1002/suco.202000488
39. Bosco C, Debernardi P. Influence of some basic parameters on the plastic rotation of reinforced concrete elements. CEB-Fib Bulletin d'Information No 218, 248, 25–44. 1993.
40. European Commitee for Standardization. Precast concrete products - test method for metallic fibre concrete- Measuring the flexural tensile strength. British Standards Institute. 2005.
41. Dassault Systèmes Simulia. Abaqus CAE User's Manual (6.12). Manuals. Providence: Dassault Systèmes. 2012.
42. Jamshidi M, Hoseini A, Vahdani S, de la Fuente A. Numerical-aided design of fiber reinforced concrete tunnel segment joints subjected to seismic loads. Constr Build Mater. 2018;170:40–54.
43. Nana WSA, Bui TT, Limam A, Abouri S. Experimental and numerical modelling of shear behaviour of full-scale RC slabs under concentrated loads. Structure. 2017;10:96–116. https://doi.org/10.1016/j.istruc.2017.02.004
44. Nogales A, de la Fuente A. Numerical-aided flexural-based design of fibre reinforced concrete column-supported flat slabs. Eng Struct. 2021;232((December 2020)):1–24. https://doi.org/10.1016/j.engstruct.2020.111745
45. Qin R, Zhou A, Lau D. Effect of reinforcement ratio on the flexural performance of hybrid FRP reinforced concrete beams. Compos Part B Eng. 2017;108:200–9. https://doi.org/10.1016/j.compositesb.2016.09.054
46. Carpinteri A, Corrado M, Mancini G, Paggi M. Size-scale effects on plastic rotational capacity of reinforced concrete beams. ACI Struct J. 2009;106(6):887–96. https://doi.org/10.14359/51663190
47. Hillerborg A. Fracture mechanics concepts applied to moment capacity and rotational capacity of reinforced concrete beams. Eng Fract Mech. 1990;35(1–3):233.
48. Pecce M. Experimental Evaluation of Rotational Capacity of HPC Beams. *CEB Bulletin d'Information No. 242, Comité Euro-International Du Béton, Laussane*, 197–210. 1997.
49. FIB Bulletin 83. Precast tunnel segments in fibre-reinforced concrete. Lausanne, Switzerland: Federation internationale du béton; 2017.

AUTHOR BIOGRAPHIES

Alejandro Nogales, PhD Candidate, Smart Engineering Ltd., UPC Spin-Off. Civil and Environmental Engineering Department, Universitat Politècnica de Catalunya (UPC), Barcelona, Spain. Email: alejandro.nogales@upc.edu

Nikola Tošić, Postdoctoral Fellow, Civil and Environmental Engineering Department, Universitat Politècnica de Catalunya (UPC), Barcelona, Spain. Email: nikola.tosic@upc.edu

Albert de la Fuente, Professor, Civil and Environmental Engineering Department, Universitat Politècnica de Catalunya (UPC), Barcelona, Spain. Email: albert.de.la.fuente@upc.edu

How to cite this article: Nogales A, Tošić N, de la Fuente A. Rotation and moment redistribution capacity of fiber-reinforced concrete beams: Parametric analysis and code compliance. Structural Concrete. 2022;23:220–39. https://doi.org/10.1002/suco.202100350